



Experimental Investigation of High-Angle-of-Attack Aerodynamics of Low-Aspect-Ratio Rectangular Wings Configured with NACA0012 Airfoil Section

Seok Ho Lee¹ · Yong Oun Han¹

Received: 5 April 2019 / Revised: 1 September 2019 / Accepted: 5 September 2019 / Published online: 13 September 2019
© The Korean Society for Aeronautical & Space Sciences 2019

Abstract

To examine the high-angle-of-attack (AOA) aerodynamics, the conventional lift and drag were measured in one revolution AOA by the dynamic load cell in the wind tunnel for rectangular wings of the NACA0012 section with four different aspect ratios, 3, 4, 5, and 6, at a Reynolds number of 1.0×10^5 . The results were analyzed in the normal and reverse modes of the airfoil. It was found that the reverse airfoil is disadvantageous to the lifting device because of the earlier stall than the normal and the substantial drag increases before the stall. In the entire AOA range, Prandtl's lifting line theory seems to be applicable in general, but the profiles of the lift coefficient are not linear anymore. It was also found that the drag coefficient of the normal airfoil mode is affected by the delta wing-type vortex wrap as well as the downwash, and that the downwash effect was dominated between the deep stall and the second peak. Using the expanding scales, which have an exponential decay rate with the aspect ratio, the polar plots of the four different wings overlap in one circle with a radius of 1.0 at the same origin.

Keywords Wind tunnel experiment · High angle of attack · Lift and drag coefficients · Aspect ratio · Polar plot

1 Introduction

Classical wing aerodynamics [1, 2] has mostly been studied considering a very low angle of attack (AOA) before the stall. However, the extended usage of the functional wing, the wind turbine [3–6], an unmanned air vehicle, and an acrobatic maneuvering plane requires more information regarding the aerodynamic behavior at the extreme AOA and regarding the corresponding dynamic motion. Because an unmanned plane requires a relatively less strict stability in flight control compared with the conventional air vehicles, any device for inducing a drastic aerodynamic change at a very high AOA can provide useful and efficient maneuverability to such a specific aimed air vehicle [7]. Therefore, the unveiled aerodynamics at an extremely high AOA, including the reverse airfoil, must be studied.

The investigation of the high-AOA aerodynamics has been attempted by two-dimensional (2D) wings as well as

finite wings. A recent study [8] found that, in a 2D wing, the interaction between the leading and trailing edge vortices plays a key role in inducing the stall, deep stall, and second peak of the lift coefficient. It also indicates that the aerodynamic data of any 2D experiment inevitably include contaminants arising from the corner effect or vortex between the wing end and the wind tunnel wall. At an AOA lower than the stall, the corner effect plays a minor role; however, as the AOA increases, it becomes a severe contaminant to the aerodynamic data. Some previous data frequently show these contaminants. The 2D experiments conducted by the wind turbine group demonstrated that C_L is frequently non-zero even at 90° or 180° AOA [9–12].

Because an experiment using the infinite span wing is not realistic in the laboratory scheme, a rather long-span finite wing would practically provide data close to the real value. A long-span wing of the glider or any blade of a vertical wind turbine, which has an aspect ratio (AR) of more than 15, shows a minor tip loss, which is practically about 5% of the lift power at a lower AOA [13]. However, in the airplane, whose AR ranges from 5 to 9 at best, the tip effect introduces severe penalty to the aerodynamic data even at a lower AOA. At a higher AOA, tip vortices become strong contaminants to both lift and drag. In a low-AR wing, such

✉ Yong Oun Han
yohan@yu.ac.kr

¹ School of Mechanical Engineering, Yeungnam University, Gyeongsan, Korea

as a super-sonic flight vehicle [14], a pair of tip vortices tends to move its trails inside, making a strong conical wrap and develop into wing vortices lingering on the suction surface to increase the lift power even at a lower moving velocity of the vehicle. Therefore, it is also interesting to observe how tip vortices affect the building of aerodynamic forces of a low-AR wing depending on the AOA change.

Therefore, to examine the tip effect with AR, a finite wing experiment in the laboratory scheme is inevitable. However, this experiment frequently tends to include more contaminants from the support or any AOA control mechanism, and the isolation of pure aerodynamic data from these contaminants is extremely difficult [15]. The lower AR wing worsens at this point, and it has a substantial contaminant owing to the tip effect. Therefore, it is important to determine the origin of the contaminant with a variation in AR as well as AOA.

In this study, the effect of AR on the aerodynamic behavior of a straight wing is experimentally investigated using four different AR wings and dynamic balance in the wind tunnel. In particular, compositions of lift and drag arising from the tip effect are monitored using the asymptotic behaviors depending on AR as well as AOA. As one of the analyzing tools, the famous Prandtl's lifting line theory is revisited and applied to understand the tip effect of the finite wing at a high AOA. In addition, the similarity of polar plots is considered to for generalization in the entire AOA range.

2 Experiments

2.1 Wing model and angle control device

The experiments were performed in a suction-type wind tunnel, which had a contraction ratio of 6:1, a squared duct with

a test section of $1.2 \times 0.9 \times 3.3 \text{ m}^3$, an inlet turbulent intensity of 0.5%, the flow angularity of 3° at the centerline and the non-uniformity of 1% at the entrance of the test section, and a maximum velocity of 25 m/s, with the axial fan driven by a three-phase 35 kW AC motor. The symmetric wing with a chord length of 0.15 m, configured with an NACA0012 airfoil section, was selected to investigate the tip effect using four different ARs, 3, 4, 5, and 6, within the width limit of the wind tunnel test section.

The model wing was mounted to the hinge at the end of a vertical pipe-type supporting jig, through which an angle control linkage passed. The AOA was controlled by a stepping motor and a connecting belt with a resolution of 0.72° at a speed of 0.1 rpm in a continuous measuring mode. The whole unit, including the supporting jig and the angle controller, was installed on the platform located at the base panel of the test section and connected rigidly to the six-component strain gage-type dynamic load cell placed underneath the test section base, as shown in Fig. 1.

The model wings including short hinge were fabricated by the 3-D printer (MakerbotReplicator2, 4G) with the PLA filament. The surface accuracy was 0.3 mm resulting 100 micron strain.

The wings were rotated at one quarter chord with a short-extended hinge, as shown in Fig. 1, and the angle was controlled through a digital input to obtain any specific AOA during two one-half revolutions of the wing. The six components' dynamic load cell (Nissho LMC6524-20) was mainly used to measure the lift and drag, with a resolution of 0.01 N and a maximum load of 20 N for both force components. Accuracy is 0.2% which corresponds to 0.04 N for the maximum load. The load range of this experiment in maximum drag measurement was 15 N for the widest AR6 wing in this study. The coupling effect is 3% and the allowable over-load is 150%.

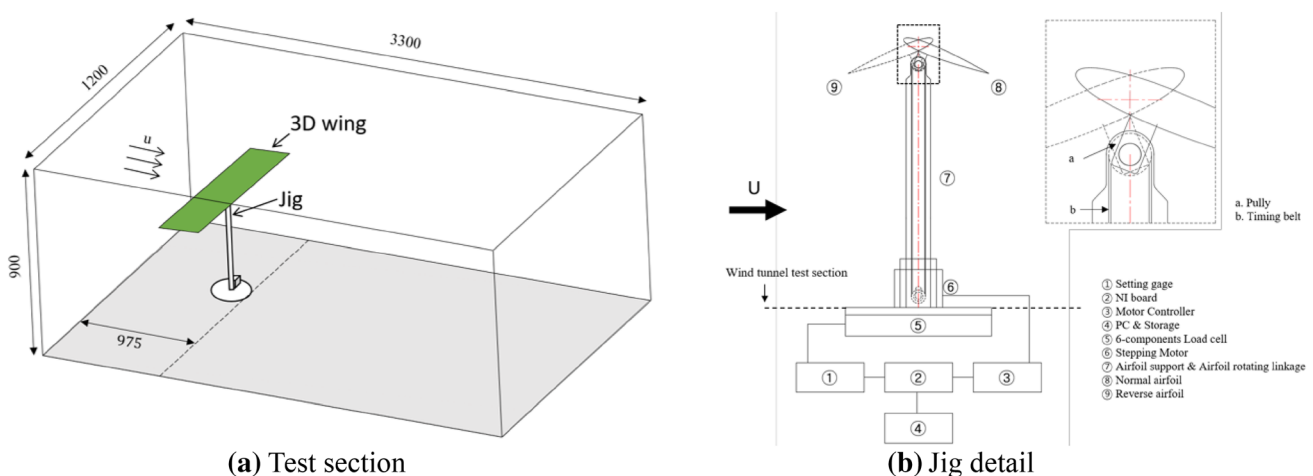


Fig. 1 Experimental layout and jig detail with instruments

The net aerodynamic forces of the wing only were obtained by subtracting the perturbed loads caused by the jig and the platform structure, and used for all data analyses in this study.

The data were acquired as electric signals and magnified by amplifiers. They were filtered using low-pass filters with 1 kHz cut-off frequency and rescaled after conditioning. To obtain the ensemble average at a given measurement point, the integral time scale was estimated, and a proper sampling rate was chosen at 200 Hz for the most disturbed condition. The conditioned data were recorded in a PC through a 15-bit A/D board installed in it and converted to physical data with calibration relation.

2.2 Error analysis

Because the data were obtained through the route composed of dynamic load cell, the angle controller, and data acquiring-recording device, the accumulated error bounce could be estimated by the following three steps. First, the force reading accompanied the error bounce from the load cell at a given upstream velocity of 10 m/s. The non-dimensional aerodynamic forces are defined by Eq. (1), and they can be expressed as a function of Reynolds number and AOA, which is α for a given upstream velocity in this experiment:

$$C_L, C_D = \frac{L, D}{\frac{1}{2}\rho U^2 A} = f(\text{Re}, \alpha). \quad (1)$$

From the equation, the final readings of the lift and drag coefficients included the uncertainty caused by the load cell and the upstream velocity perturbation. The forces and upstream velocity caused an error bounce estimated by the following relation for a given Reynolds number and AOA in these experiments:

$$\Delta f = \left| \frac{\partial f}{\partial L} \right| dL + \left| \frac{\partial f}{\partial U} \right| dU, \quad (2)$$

where the non-dimensional aerodynamic coefficient, f , ranges up to 1.0, and the lift and drag forces are less than 15 N in these experiments; therefore, the absolute values of the coefficient gradient to the load become approximately 0.067. In addition, the coefficient gradient to the incoming velocity, U of 10 m/s becomes approximately 0.1. The lift or drag force may have a disturbance equal to the accuracy of the load cell, ± 0.04 N, and the upstream also includes a disturbance, ± 0.005 of the upstream velocity in the test section of the wind tunnel. Therefore, the accumulated error bounce becomes ± 0.0027 at the maximum. Second, because the AOA controller has a resolution of 0.72° , it may cause to misread the force. In a previous study [8], the maximum slope of the lift coefficient appeared in the linear AOA

range before the stall and that of the drag coefficient at 45° AOA. Therefore, the angle resolution of both coefficients could cause the misreading of the maxima ± 0.05 at their maximum slopes. Finally, besides the independent sampling criterion, the increase in the number of samples helped in acquiring accurate meaningful data. The possible error limit, ε , with respect to the number of samples at a given grid point may be estimated by the following well-known relation [16]:

$$\frac{1}{\sqrt{N_{\text{eff}}}} \sqrt{\frac{\{\text{var } f\}}{f^2}} = \varepsilon, \quad (3)$$

where N_{eff} is the effective number of samples, f is the force, and $\{\text{var } f\}$ is the variability of the force at a fixed grid point. In these experiments, 2000 points were chosen for obtaining meaningful averages. The variability in force measurement is 0.01; therefore, the maximum error limit from the sampling criteria becomes 0.0023, which is less than 0.3%.

Therefore, the maximum accumulated uncertainty in these experiments can be estimated as ± 0.0555 at the first peak of the lift profile just before the stall AOA.

2.3 Experimental conditions

It is very difficult to isolate the jig effect from the data in such three-dimensional (3D) wing experiments. The perturbed reading of the aerodynamic values varies continuously depending on the AOA, because there exists an interaction between the model wing and the supporting mechanism. In this experiment, the lift was perturbed by subtracting the wind-off load which contains the wing, the jig and the platform in whole AOA range. Drag was perturbed by subtracting the wind-on load which contains the jig and the platform without the wing.

Experiments were carried out at the fixed incoming velocity of 10 m/s which provides Reynolds number of 1.0×10^5 based on the chord length. The inflow velocity was monitored by the digital manometer during the 4 h running test for each case and controlled not to deviate from the 1% of the intended velocity. And most tests have done mostly during the dawn to keep the constant room temperature as possible.

The biggest blockage in these experiments was occurred at the 90° of AR6 wing. The boundary-layer thickness at the jig location was estimated to be 0.0061 m from the wall which provides the maximum blockage ratios; 6.3, 8.4, 10.5, and 12.6% for AR3, AR4, AR5, and AR6, respectively. Of course, they vary depending on AOA. The cases to have more than 10% of the blockage ratio; AR5 and AR6 may bring about possible biased error in force reading near the vertical face of wings caused by the wake distortion.

Another challenging problem was the effect of the periodic coherent structure generated by the interaction

between the nose-down reverse wing and the jig. This periodicity was appeared in a short range of AOA near 150° and induced to vibrate the wing-jig unit with rather substantial energy. The frequency response of this periodicity was checked at 150° and plotted in the Fig. 2 which shows a substantial energy near 0.17 Hz with corresponding Strouhal No. of 0.0026. Except this short AOA range, such a periodicity was not detected for whole range of AOA including the normal wing.

Another periodic flow interaction between the model-jig unit and the test section wall frequently develops a sound effect so-called ‘organ effect’, especially for a high blockage experiment. However, even for AR6 wing in this experiment, the organic effect was not detected.

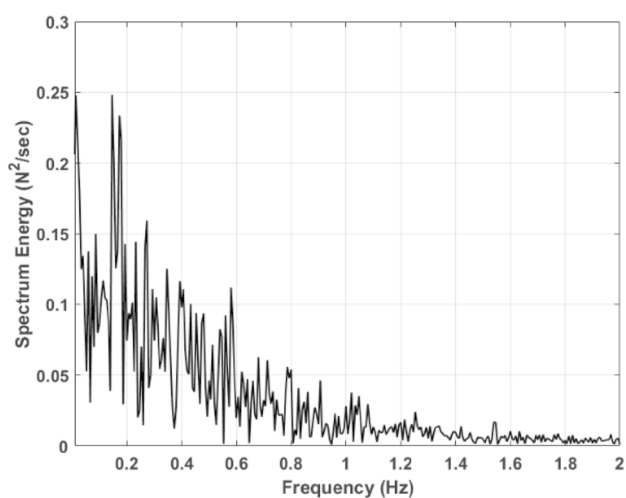
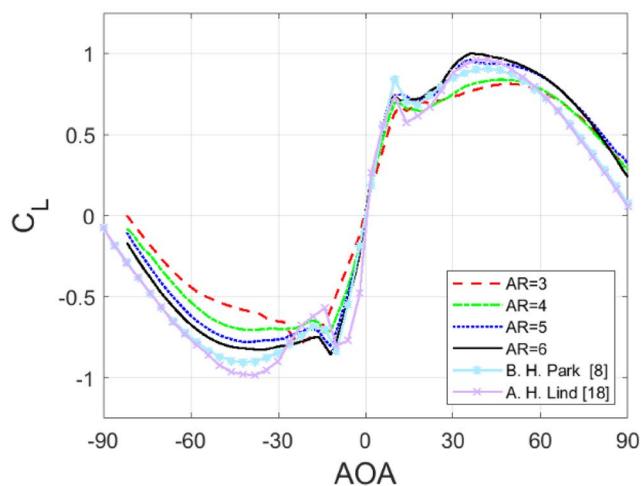


Fig. 2 Frequency response of the nose-down reverse wing of AR5 at 150° of AOA



3 Results and discussion

3.1 AR effect

The experiments are carried out for two sets of airfoil modes: a normal mode of -90° to $+90^\circ$ AOA [17] and a reverse mode of 90° to 270° AOA. Note that two separate sets of experiments are inevitable in such a 3D wing measurement because of the obstruction by the supporting mechanism and the force reading jig, whereas a continuous one revolution of AOA is possible in the 2D measurement [8, 18].

Figures 3 and 4 show the results for the lift and drag coefficients for the four AR wings. In Fig. 3, in the low-AOA range, the lift profiles of all finite wings are observed to be lesser than those in the 2D numerical case, including the first peaks, but the trend reverses in the high-AOA range. Note that C_L curves at 90° AOA, where the wings have nose-up vertical poses, are not reached at the horizontal axes; owing to some reasons, they seem to cross at more than 90° AOA, whereas both 2D cases are close to. This phenomenon takes place similarly at another nose-down vertical pose of the 3D wings, where they seem to reach the crossing points before -90° AOA. This explains that there are obstructive jig effects to break the symmetry with respect to the zero C_L . The downwash over the nose-up wing develops favorably even at a high AOA, while the upwash over the nose-down wing is definitely obstructed by the jig. These results imply that the actual C_L value is fairly dependent on the downwash induced by the conventional tip vortices, which leave soon after being generated by the wing tip in the low-AOA range.

For all AR wings, the first peaks coincide near 10° AOA with an increase in C_L as AR increases. However, the second peaks start at 55° of AR3 and seem to converge to 40°

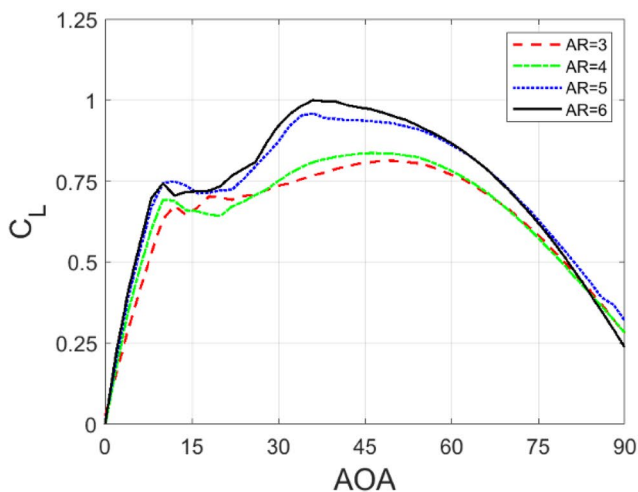


Fig. 3 Lift coefficient profiles of the normal wing (left) with 2D results and those of nose-up wings (right)

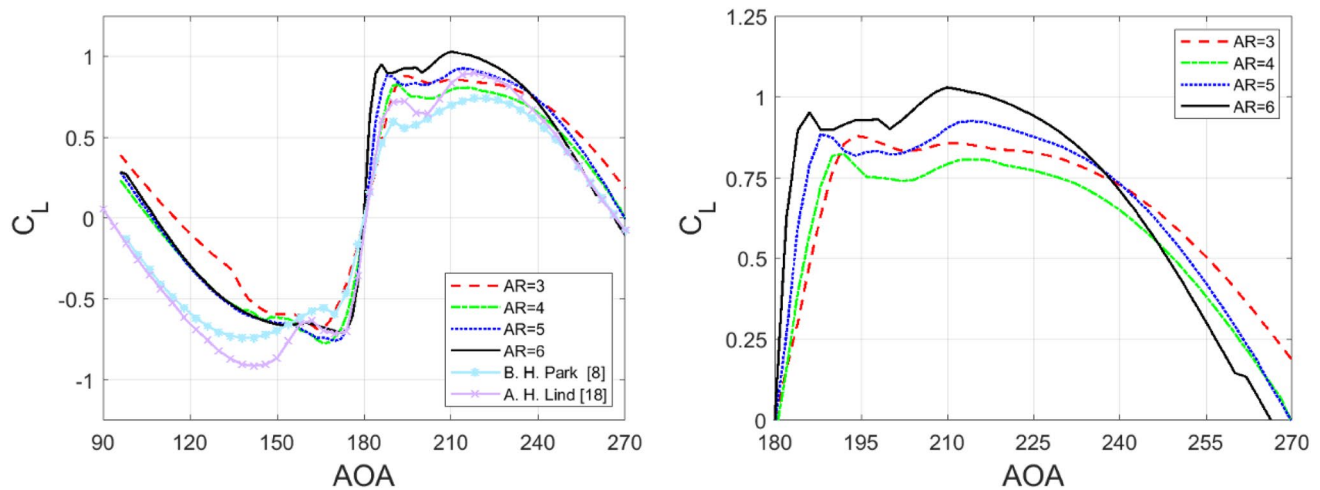


Fig. 4 Lift coefficient profiles of the reverse wing (left) with 2D results and those of nose-up wings (right)

for high-AR wings. The second peak of the 2D wing was previously reported to appear at 42° AOA [8, 18]. The present data indicate that the second peak of the high-AR wing occurs earlier than the 2D case with a higher lift, but the low-AR wing has the second peak near 50° AOA, later than the 2D case with less value, as well. From this observation, it is easily inferred that the force difference between the 2D and 3D wings is caused by an uncertain effect besides the downwash. This uncertain effect seems to be an additive hauling force caused by a pair of soared tip vortex wraps above the suction surface, such as a delta wing [14] in the high-AOA range, similar to side rolls appearing on a vertical plate. A detailed interpretation will be presented in the next section. These observations indicate that the higher AR wings are affected mainly by the downwash in most AOA ranges, while the low-AR wings are dominated by the tip vortex wrap despite having the downwash effect. Therefore, the higher AR wing seems to have an advantage in obtaining the higher second peak for the high-AOA flight device, even for such a limited number of AR samples.

In Fig. 4, all nose-up reverse wings provide higher lift than the 2D wing and their second peaks appear near 30° . All reverse wings look dominated mainly by the downwash in the whole range of AOA, because their second peaks appear before 45° . Compared with the normal cases, the tip vortex wrap weakens near the blunt tail edge; therefore, it does not influence the reading of C_L as much as the normal cases. Another noticeable fact is that, compared with the normal cases, the stall occurs at an earlier AOA with AR with an increasing magnitude, as shown in the figure. This indicates that the tip vortex generated by the sharp leading edge has an early influence in the creation of the downwash, compared with the normal mode at the corresponding AOA. This explains why the reverse wing is not applicable to a lifting device, because it induces earlier stall than the normal.

Another interesting observation occurs at 240° AOA, which corresponds to 60° AOA for the normal wing. All C_L values are read the same, because the effects caused by both the trailing edge vortex and the tip vortex wrap become balanced. There seems to be a complicated flow interaction near the tail edge proximity caused by the vortex interaction at high AOA [8]. In the AOA range of the nose-down airfoil mode, the upwash seems to be influenced by the jig effect. To separate such a jig effect, an upside-down experimental set would provide for the future experiment.

It is also interesting to examine the C_D results in detail, as shown in Fig. 5. The normal wing has the benefit of a low AOA, approximately 0° to $+10^\circ$ for ARs 4, 5, 6 cases, where the drag reads almost zero before the stall even in the cases of the nose-down mode. However, the C_D profile of the reverse wing does not have the zero drag zone, even in the lower AOA range. The rounded tail edge allows the counter-rotating trailing edge vortex to move in the upper wing surface near the tail and to make the stream line over the suction surface continuously separated [8]. Therefore, the reverse airfoil does not have advantage, especially at the low AOA. It is another factor why the reverse wing is not applicable to any lifting device besides the earlier stall, as mentioned before. A detailed discussion of the drag will be provided in Sect. 3.3.

As observed before, profiles of the lift coefficient showed a substantial asymmetry with respect to zero AOA compared to those of the drag coefficient. The Fig. 6 is made by overlapping both absolute profiles in the same absolute AOA ranges of nose-up (0° – 90°) and nose-down (0° to -90°) wings for AR6 normal wing. It implies that the jig definitely interfered to develop the upwash of the nose-down wing. It explains that even with the symmetric wing and a proper subtraction of the jig effect in force measurement for both wings, the wake interaction between the wing and the jig is

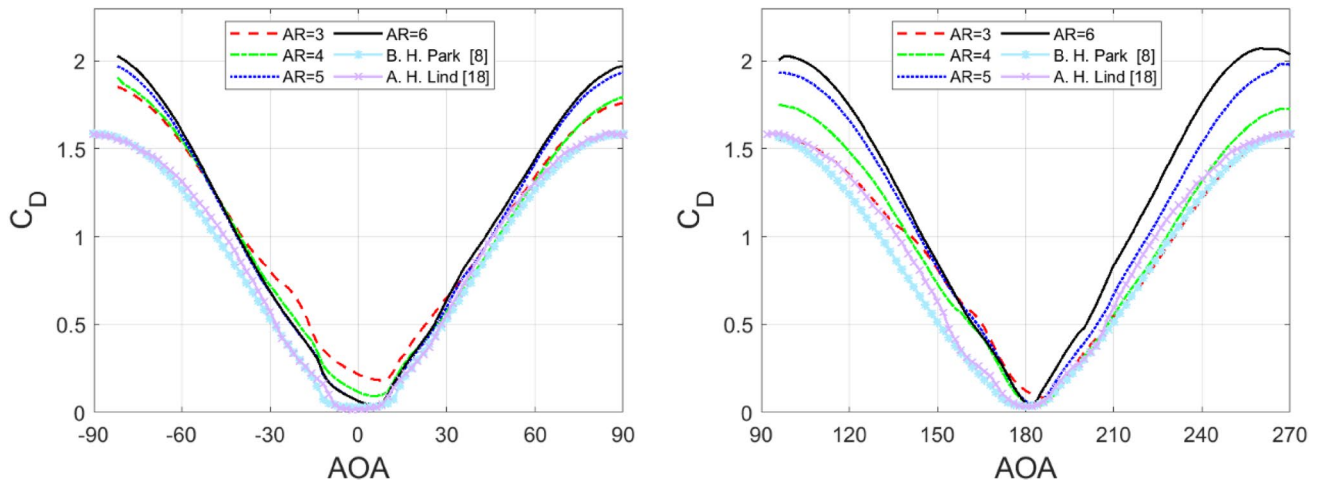


Fig. 5 Drag coefficient profiles of the normal and reverse wings for four ARs including the 2D cases

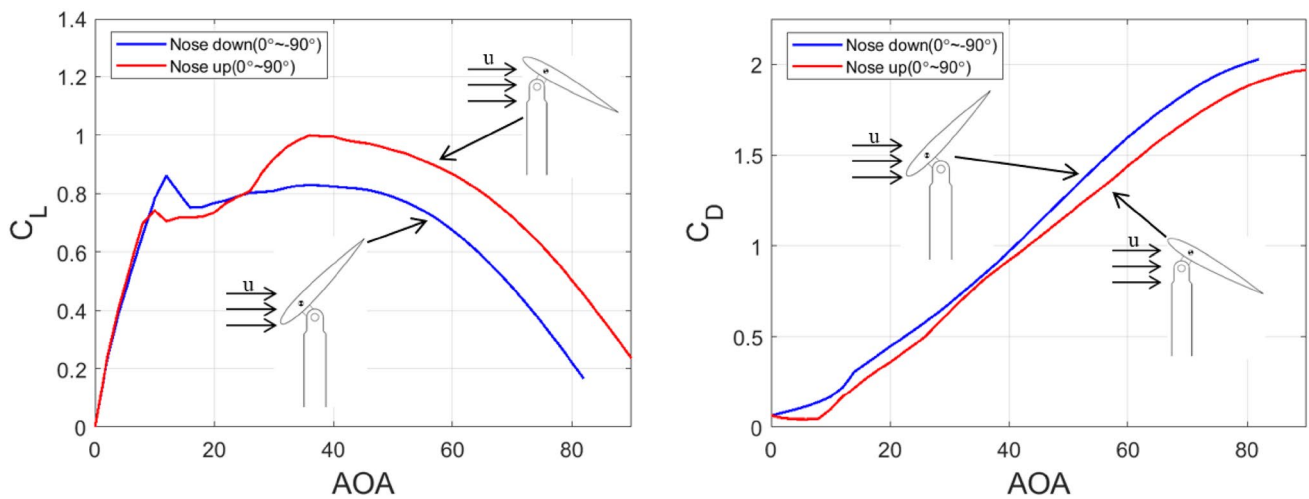


Fig. 6 Asymmetry for the lift (left) and the drag (right) coefficients of AR6 normal wing

not eliminated symmetrically which is the unique limit of the 3-D experiment. As observed to get rid of this asymmetry, another set of upside-down experiment could be an only way to solve this trouble. By combining two half data, it is expected to complete the uncontaminated data set during one revolution of AOA. But even with such defect, the general behavior of aerodynamic characteristic using two separated half revolutions seems to be obtained. Such an asymmetry gets reduced as AR increases definitely.

Another interesting thing is observed in profile of C_D in the low-AOA range of the normal wing, as shown in Fig. 7. Compared to the numerical and the 2-D experiment cases, the C_D value of 3-D wing lessens slightly with increase of AOA until the stall. It implies that there exists the horseshoe vortex, or the corner vortex at the junction between the jig-end and the wing which contributes to generate a certain

amount small drag at zero angle, but is soon suppressed as AOA increase resulting to reduce the drag slightly. This also seems to be a unique feature of 3-D experiment which may not be eliminated.

3.2 Real AOA of 3D wing

The AOA is defined as the angle between the moving axis and the chord line of the symmetric airfoil; however, the real AOA of the 3D wing depends on various factors, such as airfoil shape, pressure distribution over the wing surface, downwash, and tip vortex wraps. It is interesting to examine the resulting force direction, which is divided into the actual lift and drag in a conventional manner. Hence, the additional moment, nose-up or nose-down, more than expected at the given posture of the wing may be obtained.

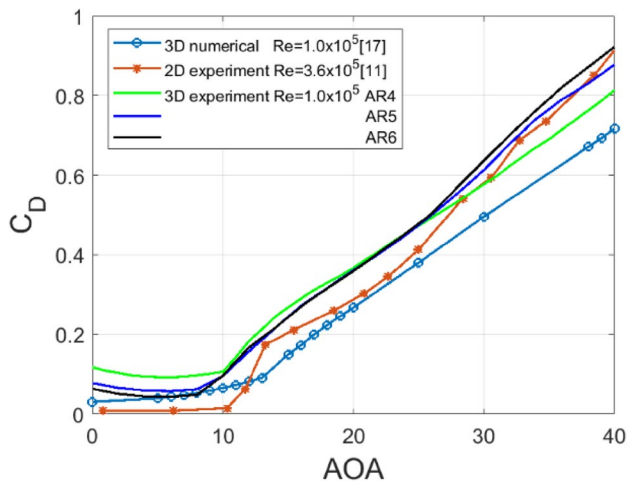


Fig. 7 Drag coefficient of the AR4, 5, 6 normal wing in low-AOA range

At a high AOA, the resulting force direction over the wing is the key factor for designing the high-angle vehicle. A low-AR wing is dominated by the tip vortex wrap as well as by the downwash, whereas the high-AR wing tends to be dominated mainly by the downwash, which becomes the only effect as AR tends to infinity. To examine the portion of the two effects, the following angle can be used to check the balance. A real AOA defined by the following relation can provide interesting physics around the airfoils:

$$\alpha' = \frac{\pi}{2} - \tan^{-1} \frac{L_m}{D_m}; \quad 0 \leq \alpha' \leq \frac{\pi}{2}, \quad (4)$$

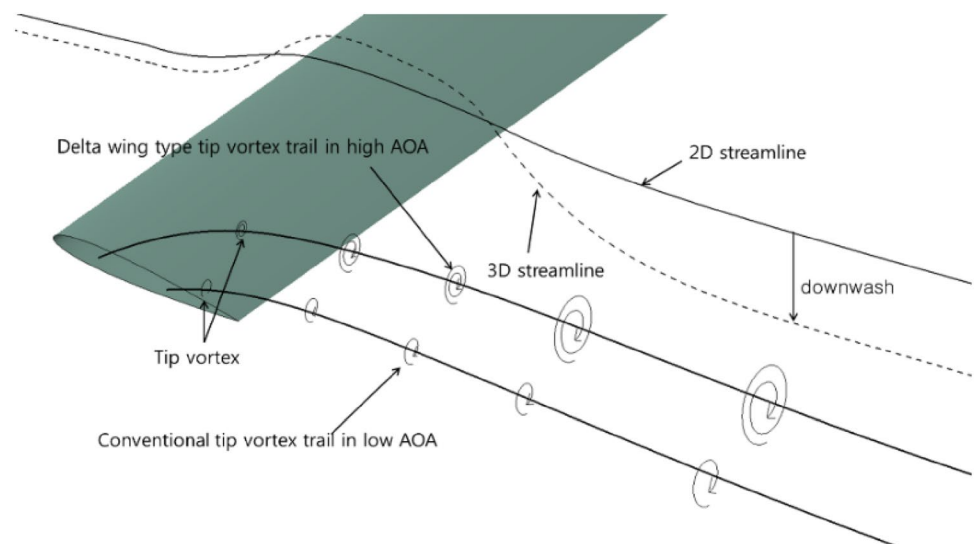
where L_m and D_m are vertical and horizontal components of the resulting force, respectively, measured directly in this experiment.

As described before, a finite wing builds downwash in a normal nose-up wing by the tip vortex pair shown in Fig. 8. The downwash effectively induces the real AOA to be a little higher than the geometric AOA, which causes an increase in the drag, called induced drag, as well as the corresponding penalty of the lift. The tip vortex pair plays two roles to read the aerodynamic forces: to generate the downwash in a moderate low range of AOA and to create an additive hauling force when the vortex pair stays behind the wing in the high-AOA range, just like a delta wing, as depicted in Fig. 8. As AR increases, the only downwash effect is dominated and disappears in a high-AR wing, even a 2D wing. However, in a realistic size of AR, two effects always exist in the whole range of AR. Especially, the low-AR wing has two distinctive AOA ranges. Therefore, it is useful to define a real AOA, α' , which explains well the composition of these two effects depending on the AOA range.

To compare the real force composition of this 3D airfoil, a theoretical zero-thickness flat plate wing is chosen as the base wing. A previous study [19] provided an asymptote using the experimental result from various ARs of flat plates.

The normal mode wing is depicted in Fig. 9 (left), which shows that the real AOA of the 3D wing tends to coincide with the flat plate at 45° AOA. As soon as the lift obtains at the small positive AOA, the resultant force direction becomes more vertical to the moving direction, which is beneficial until the stall angle and deep stall angle are reached. Note that in the AOA range between the deep stall and the second peak, the resultant force of most wings slightly inclines to the tail direction compared with the theoretical flat wing. This indicates that the curvature of the streamline vibrantly induces the downwash effect in this high-AOA range, so that the real AOA increases beyond the geometrical AOA of the wing platform, resulting in additional nose-up moment to the wing. However, after these

Fig. 8 Schematic of tip vortex trails and streamlines of 2D and 3D wings



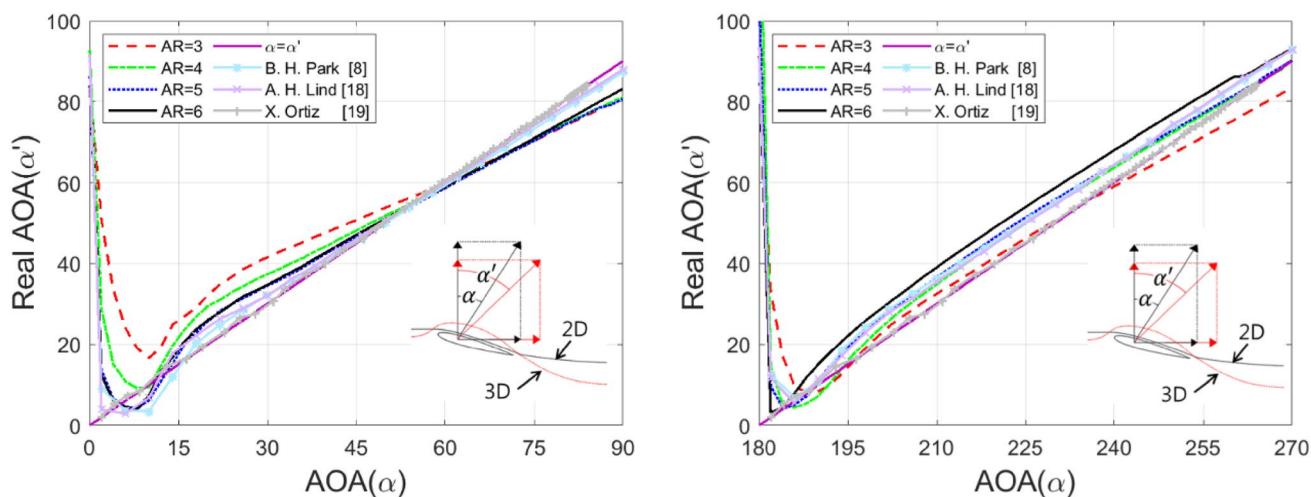


Fig. 9 Real and geometric AOAs of normal (left) and reverse (right) wings with 2D wings and a flat plate case

angles, the reverse fact occurs, because the tip vortices wrap around the suction surface, which induces more lift than that expected, similar to the delta wing at high AOA. Conclusively, when the wing has a lower real AOA than the flat plate, it tends to have a little higher nose-down moment than that expected, partly because of the vertical force direction before the stall angle and partly because of the lingering vortex wrap on the suction surface near the tail at high AOA.

The reverse-mode airfoil provides different features, as shown in Fig. 9 (right). The AR3 wing is dominated by the tip vortex wraps in most of the AOA range. A very low-AR wing cannot develop the downwash effect, partly because it has relatively strong vortex wraps and partly because the blunt trailing edge hardly contributes to development of the downwash. As reported in [8], the blunt tail allows the trailing edge vortex to move upward, staggering near the tail, so that it blocks the development of the downwash. However, the high-AR wings are much dominated by the downwash in the whole range of AOA, except the AR3 wing, because its blunt tail edge cannot generate a trailing edge vortex strong enough to break the downwash effect.

3.3 Induced drag of the finite wing

Prandtl’s lifting line theory [20] contributed to the development of the 3D slender airfoil aerodynamics in the low-AOA range. In his previous studies, he found that the lift coefficients obtained from the different ARs tend to overlap in a single straight line and converge to the 2D airfoil eventually at low AOA, and indicated that the drag coefficient of the 3D wing can be expressed in terms of 2D drag and the induced drag. In those days, the researchers were not interested in high-AOA aerodynamics. Extension of this theory to the high-AOA range may provide useful results, irrespective of

whether the theory still holds or not. In this study, Prandtl’s experiment is revisited up to 90° AOA only for the normal wing. Of course, it is applicable to all airfoil modes, including the nose-up and down poses, as far as the jig effect is expelled effectively.

In this experiment, the highest AR was 6, whereas he used AR7 for the longest airfoil. All four lift coefficients were redistributed using Eq. (5) with respect to the AR6 case and plotted in Fig. 10:

$$C_{L,i} = C_{L,i-1} + a \times \frac{\pi}{180} (\alpha_i - \alpha_{i-1}), \tag{5}$$

where a is the slope of the linear profiles before the stall.

As a result, there seems to exist a similarity for all four AR cases up to 90° AOA. As Prandtl examined in his

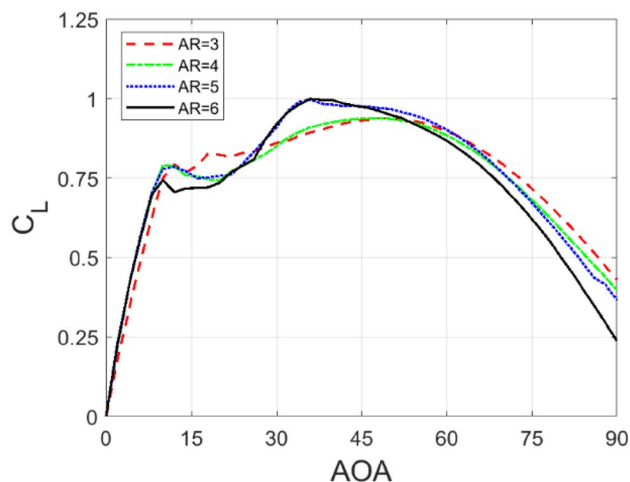


Fig. 10 Overlapped C_L profiles of four AR wings for the normal nose-up mode

experiment, the overlapped profiles before the stall appear linear. In addition, over the extended range of AOA, a similarity seems to exist in general; however, the whole profile is not linear any more. This implies that in a certain range of AR, the lift coefficient may have another functional relation of the variable AR.

The distinguished feature of the 3D wing from the 2D wing is the fact that the 3D wing has an induced drag from the downwash generated by a pair of tip vortices. Prandtl suggested that, in a low-AOA range, the total drag comprises the 2D drag, obtained from the experiments [20, 21], and the induced drag part, defined by the second term of Eq. (6) [22]. Here, the induced drag can be estimated using the measured C_L , span factor e , and AR:

$$C_D = c_d + \frac{C_L^2}{\pi e AR} \tag{6}$$

The span factor e indicates a taper ratio of the 3D wing for a given AR. Prandtl derived e using Eq. (6) reversely. To extend his theory to the entire AOA range up to 90°, the induced drag was calculated by the second term. The total drag was obtained using this equation with a span factor of 0.94–1.00 for a rectangular wing, according to McComick [23], and their results are plotted in Figs. 11 and 12. The AR6 wing showed the maximum induced drag to be about 8.6% of the total drag near 35°, and that the AR3 wing had a value of 7.8% near 50°, and both maxima were in their second peaks, as shown in Fig. 11.

Figure 12 shows the profiles of the total drag calculated using Eq. (6) and that measured directly for different AR wings in this experiment. To estimate the 2D drag coefficient, $C_{d,2D}$, the previous calculation conducted by [8] is used. The plot explains that the experimental results of high-AR wings well-match Prandtl’s extension up to the second peak

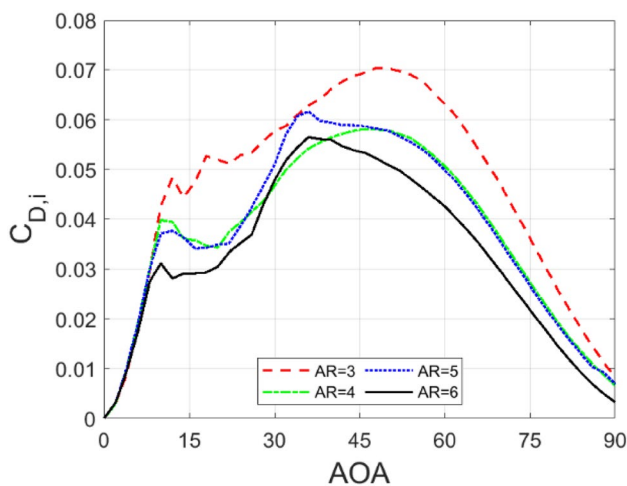


Fig. 11 Induced drag coefficients estimated

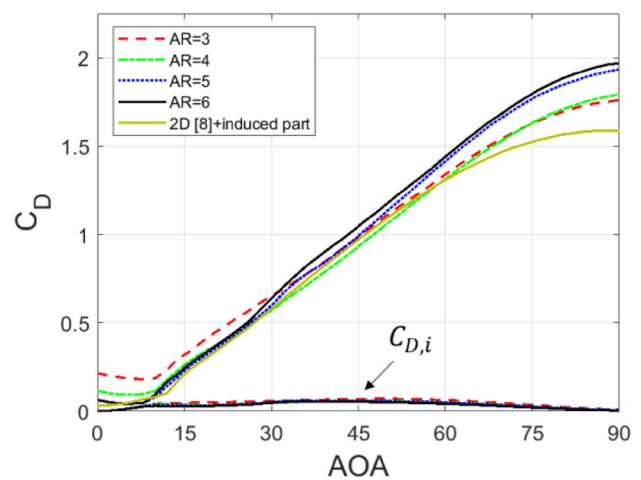


Fig. 12 Total drag estimated and measured for different ARs

or approximately up to 50°; however, they considerably deviate from the estimation in the higher AOA range. This also indicates that at a higher AOA, the delta wing-type vortex wrap promotes more drag in the experiments, as mentioned before. The low-AR wing shows much deviation in the whole AOA range, which means that the low-AR wing can be easily contaminated by the delta wing-type vortex wrap, as observed in the lift part.

Note also that the induced drag becomes substantial in the second peaks; however, its contribution to the total drag reduces as AR increases, as shown in Eq. (6). This also explains that as AR increases, the role of the induced drag decreases, because the tip loss caused by the tip vortex roll relatively lessens. This observation made so far summarizes that Prandtl’s lifting line theory holds at least until the AOA of the second peak of the lift coefficient for a higher AR wing.

3.4 Similarity of polar plot

The lift-to-drag ratio provides the effectiveness of the wing in a certain range of AOA. The measurement results obtained using four different AR wings are plotted in Fig. 13 for both the normal mode and the reverse mode, including the 2D results and the flat plate experiment. Except for the narrow bands, -15° to $+15^\circ$ for the normal mode and 165° – 195° for the reverse mode, the profiles collapse in a simple monotonous curve. This indicates that, in the AOA range more than the deep stall, profiles of all AR wings overlap into a rigid asymptotic curve. The symptom of such a similarity profile is already presumed in the whole C_L profile, as observed in the extension of Prandtl’s idea before.

It is meaningful to obtain an asymptotic relation from the remaining data, except the narrow-AOA bands. Based on the present data shown in Figs. 3 and 4, it is granted that

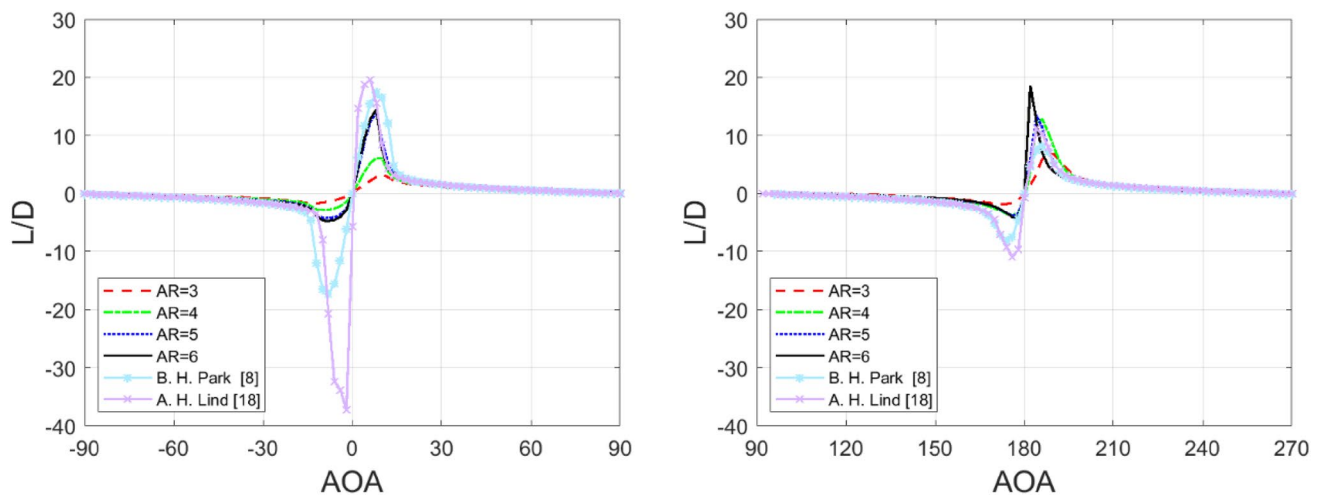


Fig. 13 L/D ratios of the normal and reverse wings including 2D wings

Table 1 Maximum C_D and C_L peaks of NACA0012 2D airfoils

$C_{l,1st}$	$C_{l,2nd}$	$C_{d,max}$	Re	References
–	–	2.05	9.5×10^5	[12]
1.33	1.15	2.08	1.8×10^6	[9]
1.08	1.13	1.95	5.0×10^5	[9]
–	–	2.08	3.0×10^5	[24]
0.73	0.96	1.59	1.1×10^5	[18]
0.89	0.91	1.59	1.0×10^5	[8]
1.11	1.09	1.89	7.6×10^5	[10]
1.07	1.08	1.80	7.0×10^5	[12]

the lift coefficient increases up to 1.0 for the nose-up airfoils of both normal and reverse wings at the second peaks in high-AR cases. Moreover, it is expected that those of the nose-down airfoils can have the same magnitude in the negative direction if the jig effects are properly eliminated. The drag coefficient seems to have a maximum value of 2.0 for both airfoil modes, as shown in Fig. 5. Considerable previous data of the NACA0012 section wings support that the maximum C_D may be close to 2.0 at the vertical poses of the wings, as listed in Table 1. The 2D vertical flat plate experiences a maximum drag coefficient of 2.0 by applying a simple momentum theory. The data may be differing slightly depending on the Reynolds number.

The polar plot is used as a convenient tool to understand L/D ratio for one revolution of AOA. It can be used to decide whether the similarity exists, depending on the AR change in the whole range of AOA. By rescaling the profiles of the lift and drag coefficients measured in the present study, the similarity is examined by establishing the asymptote. As seen in the measured data, both profiles

of lift and drag converge to those of the high ARs. The scale factor, S , required to meet a simple asymptote by expanding the profiles of low-AR wings is found in the following exponential relation (7) for both airfoil modes, and the results are shown in Fig. 14. Even with the limited AR cases of these experiments, the AR6 wing is used for an asymptotic target in the whole AOA range as Prandtl used the AR7 case in the low-AOA range. To obtain a proper function, the following equation is applied to the cases. The related coefficients are also listed in Table 2:

$$S = Ae^{-AR} + B, \quad (7)$$

where A is the gain optimized from the data of these experiments and B is the offset. To obtain a proper offset B , the maxima of C_L and C_D of the previous data are used as reference.

The polar plot of the flat plate is selected as the base plot, which has a radius of 1.0 with respect to the origin (1.0, 0.0). Except for the narrow band of AOA, most profiles become close to the base plate, and their plots are shown in Fig. 15. Especially, the profile of the nose-up normal wing coincides well with the base circle, but the nose-down normal mode is much deviated, because the upwash is severely contaminated by the supporting structure. The profile of the reverse airfoil mode provides a similar result; however, the distortion of the nose-down mode becomes substantial, especially in AR3. The low-AR reverse wing seems to be severely contaminated by the tip vortex wrap, as mentioned before. Based on such an asymptotic behavior of the polar plots, the exponential decay rate of AR can be used to introduce a proper functional relation working in the whole range of AOA.

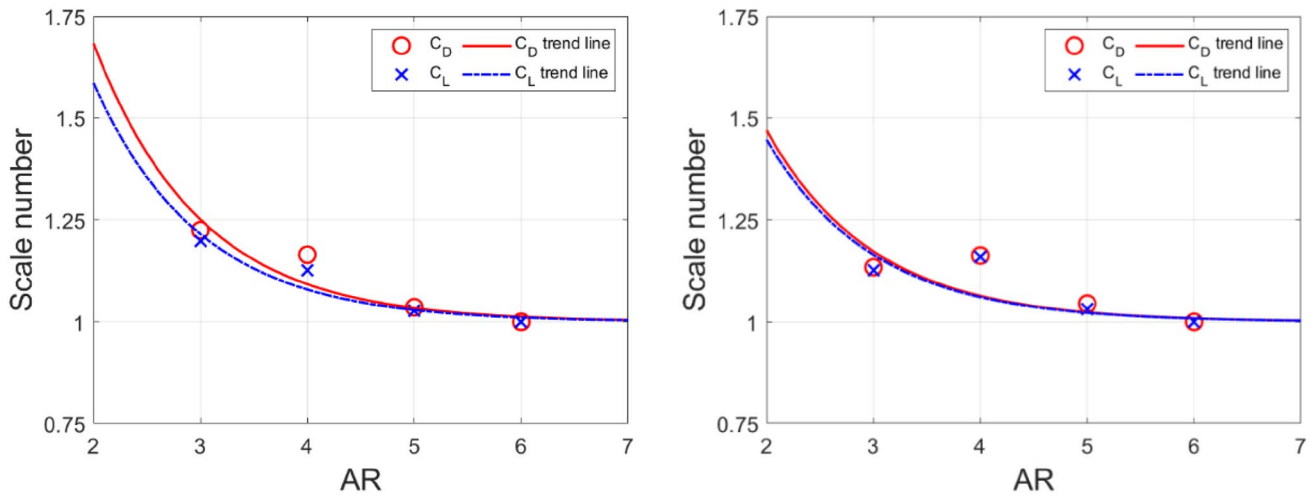


Fig. 14 Asymptotes of the normal (left) and reverse modes (right)

Table 2 Expanding scale factors and gains to obtain the asymptotes

AR and gain A	Normal		Reverse	
	C_D	C_L	C_D	C_L
3	1.225	1.1986	1.134	1.1274
4	1.165	1.1274	1.1627	1.1591
5	1.0357	1.0265	1.0445	1.0314
6	1	1	1	1
A	5.047	4.327	3.472	3.304

4 Conclusions

The aerodynamic forces of four different AR wings, which have NACA0012 airfoil sections, were measured by the dynamic load cell for both normal and reverse wings at the

Reynolds number of 10^5 . As a result, the following conclusions were drawn:

1. For a normal wing, all lift coefficients of the four AR wings have the first peaks near 10° AOA, and as the AR increases, the second peaks appear close to 40° , which appear at earlier AOA than the 2D airfoil predicted. This indicates a 3D effect induced by the tip vortices. The stall of the reverse wings comes earlier than the normal case as the AR increases, making the slope steeper. In the AOA range of 170° – 190° , the drag coefficient of the reverse wings of all ARs does not provide any zero-level profile, as shown by the normal wing. The earlier stall and the non-zero-level drag coefficient in the low-AOA range become a critical defect in the application of the reverse for airplanes. This is because the reverse wing has an earlier vortex wrap than the normal wing, and its trailing edge vortex lingers along the blunt edge.

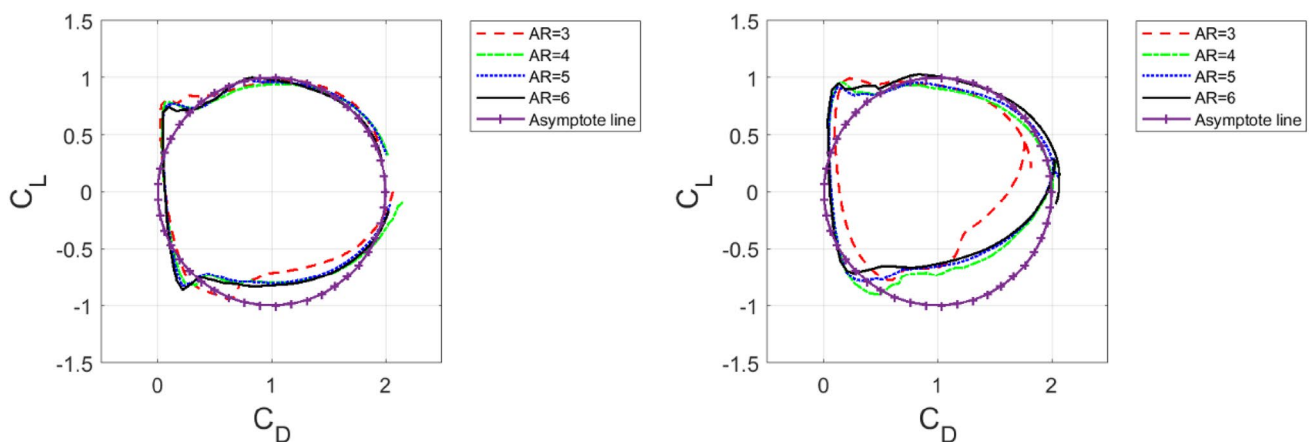


Fig. 15 Polar plots of the normal and reverse 3D wings

2. The source of the extra drag in the 3D wing originates partly from the downwash effect and partly from the delta wing-type vortex wrap. The lower AR wing tends to be contaminated by the tip vortex wrap, while the higher AR wing is considerably dependable on the downwash. The difference between the real and the geometric AOA explains the extra pitching moment related to the contaminants from the downwash and the vortex wrap. Compared with the flat wing, before the stall, the normal wing tends to have an extra nose-down moment, and between the stall and the second peak, shows an extra nose-up moment. However, except for the AR3 wing, the reverse wing seems to be contaminated by the downwash effect in the whole AOA range.
3. Prandtl's observation holds even in the higher AOA range, and the profiles of all lift coefficients collapse into one profile, showing the possibility of existence of the similarity until at least the second peak, but after the stall angle, their profiles become very nonlinear. Using Prandtl's lifting line theory, the induced drags of the four AR wings show the maximum induced drag to be 7.8–8.6% of the total drag at their second peaks.
4. The polar plots of the normal mode collapse well into one circle of radius 1.0 with the center at (1.0, 0.0) in polar coordinates by expanding the scale factors. This result implies that there exists a possibility to have an exponential function to the exponent of $-AR$ to satisfy the overall similarity in the whole AOA range beyond the limited Prandtl observation within the stall.

Acknowledgements The authors acknowledge Mr. Jae Hoon Lee for his valuable help in drawing decent graphs.

References

1. Laitone EV (1997) Wind tunnel tests of wings at Reynolds numbers below 70000. *Exp Fluids* 23(5):405–409. <https://doi.org/10.1007/s003480050128>
2. Mueller TJ, Pohlen LJ, Conigliaro PE, Jansen BJ (1983) The influence of free-stream disturbances on low Reynolds number airfoil experiments. *Exp Fluids* 1(1):3–14. <https://doi.org/10.1007/BF00282261>
3. Miley SJ (1982) Catalog of low-Reynolds-number airfoil data for wind-turbine applications (No. RFP-3387). Rockwell International Corp., Golden, CO (USA). Rocky Flats Plant; Texas A and M Univ., College Station (USA). Dept. of Aerospace Engineering
4. Holst D, Church B, Pechlivanoglou G, Tüzüner E, Saverin J, Nayeri CN, Paschereit CO (2017) Experimental analysis of a NACA 0021 airfoil section through 180-degree angle of attack at low Reynolds numbers for use in wind turbine analysis. In: ASME Turbo Expo 2017: turbomachinery technical conference and exposition (V009T49A006-V009T49A006). American Society of Mechanical Engineers
5. Bloy AW, Roberts DG (1993) Aerodynamic characteristics of the NACA 63₂-215 aerofoil for use in wind turbines. *Wind Eng* 1993:67–75
6. D'angelo S, Gili P (1988) Wind tunnel measurements of aerodynamic coefficients of asymmetrical airfoil sections for wind turbine blades, extended to high angles of attack. In: Commission of the European Communities. Contractors' meeting, vol 2, pp 297–308
7. Rival D, Tropea C (2010) Characteristics of pitching and plunging airfoils under dynamic-stall conditions. *J Aircr* 47(1):80–86. <https://doi.org/10.2514/1.42528>
8. Park BH, Han YO (2018) Steady aerodynamic and flow behaviors of two-dimensional NACA0012 airfoil in one revolution angle of attack. *Int J Aeronaut Space Sci* 119:1. <https://doi.org/10.1007/s42405-018-0010-x>
9. Critzos CC, Heyson HH, Boswinkle Jr RW (1951) Aerodynamic characteristics of NACA 0012 airfoil section at angles of attack from 0 deg to 180 deg. NACA-TN-3361
10. Michos A, Bergeles G, Athanassiadis N (1983) Aerodynamic characteristics of NACA 0012 airfoil in relation to wind generators. *Wind Eng* 1983:247–262
11. Sheldahl RE, Klimas PC (1981) Aerodynamic characteristics of seven symmetrical airfoil sections through 180-degree angle of attack for use in aerodynamic analysis of vertical axis wind turbines (No. SAND-80-2114). Sandia National Labs., Albuquerque, NM (USA). <https://doi.org/10.2172/6548367>
12. Massini G, Rossi E, D'angelo S (1988) Wind tunnel measurements of aerodynamic coefficients of asymmetrical airfoil sections for wind turbine blades extended to high angles of attack. In: European Community wind energy conference, pp 241–245
13. Leishman GJ (2005) Principle of helicopter aerodynamics. Cambridge University Press, Cambridge
14. Freymuth P, Bank W, Finaish F (1987) Further visualization of combined wing tip and starting vortex systems. *AIAA J* 25(9):1153–1159. <https://doi.org/10.2514/3.9760>
15. Pope A, Harper JJ (1966) Low-speed wind tunnel testing, 4th edn. Wiley, New York
16. George WK, Beuther PD, Lumley JL (1978) Processing of random signals. In: Proceedings of dynamic flow conference, Denmark
17. Lee JH, Han YO (2019) Numerical investigation on evolution of tip vortices generated by low-aspect ratio rectangular wings at high angle of attack. *Int J Aeronaut Space Sci* 20(1):1–13. <https://doi.org/10.1007/s42405-018-0101-8>
18. Lind AH, Lefebvre JN, Jones AR (2014) Time-averaged aerodynamics of sharp and blunt trailing-edge static airfoils in reverse flow. *AIAA J* 52(12):2751–2764. <https://doi.org/10.2514/1.J052967>
19. Ortiz X, Rival D, Wood D (2015) Forces and moments on flat plates of small aspect ratio with application to PV wind loads and small wind turbine blades. *Energies* 8(4):2438–2453. <https://doi.org/10.3390/en8042438>
20. Prandtl L (1921) Applications of modern hydrodynamics to aeronautics. NACA TR 116
21. Abbott IH, Von Doenhoff AE (1959) Theory of wing sections. Dover Publication Inc., New York, pp 462–463
22. Anderson JD Jr (2010) Fundamentals of aerodynamics, Chapter 5, 5th edn. McGrawHill, New York, pp 440–448
23. McCormick BW (1979) Aerodynamics, aeronautics, and flight mechanics, chapter 4. Wiley, New York, p 191
24. Strickland JH (1976) Aerodynamics of the Darrieus turbine. Sandia Lab Rep 76:29–58

Publisher's Note Springer Nature remains neutral with regard to jurisdictional claims in published maps and institutional affiliations.